Chapter 9

Dynamics of Ultrafast Energy Redistribution in C_{60}

Energy redistribution processes in C_{60} after the excitation with ultrashort laser pulses are the focus interests in this chapter. First, a general overview on energy redistribution processes important for the fragmentation of C_{60} fullerenes is given. Next, the experimental observations of ultrafast energy redistribution obtained with a single pulse are discussed in detail. Then, one and two colour pump-probe techniques are applied to study the energy redistribution dynamics. Finally, the control of this dynamics with judiciously tailored laser pulses is presented.

9.1 Energy Coupling

There are two dominant processes of energy redistribution in large systems: electron-electron coupling and electron-phonon coupling. These processes correspond to the energy flow within the electronic subsystem and its exchange with the nuclear degrees of freedom, respectively. However, one has to keep in mind that C_{60} is a large, but still finite molecular system with discrete energy levels and well defined modes of nuclear motion.

In a photoinduced excitation process (involving typically many absorbed photons), electronic and nuclear motion are intrinsically connected through the Franck-Condon (FC) principle. There is one notable exception in the case of C_{60}: the direct single multiphoton ionisation. There, the initial ground state potential hypersurface of the neutral C_{60} and that of the ionic ground state have a very similar structure and thus by virtue of the FC principle very little vibrational excitation is expected. All ionisation processes into higher charge states may involve the plasmon resonance which strongly couples with vibrational motion. Consequently,

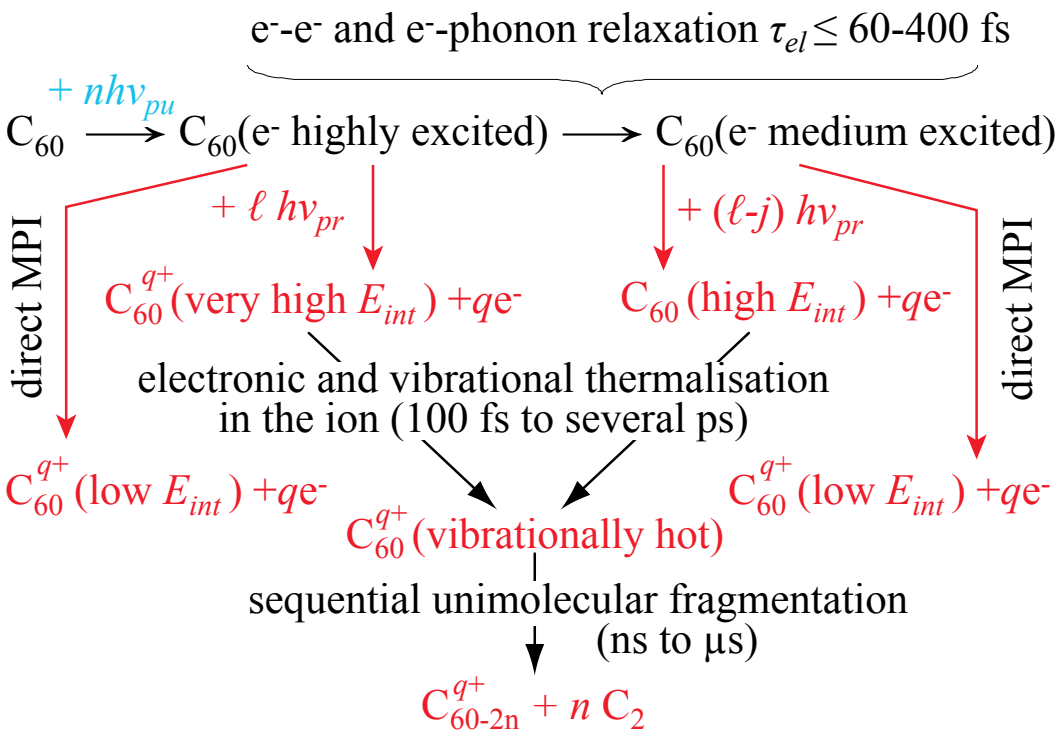

Figure 9.1: Illustration of energy redistribution processes in laser excited C_{60} molecule monitored in the present work with two colour pump-probe spectroscopy.

one can not attribute experimentally observed relaxation times to electron-electron coupling exclusively. Rather, highly excited electrons formed during an intense laser pulse will exchange energy by the combined action of electron-electron scattering and electron coupling with the various vibrational degrees of freedom of the neutral molecule. After electron-electron coupling statistical emission of electrons can occur from the excited electronic subsystem. Statistical energy redistribution among vibrational degrees of freedom leads to the observation of delayed ionisation (thermionic emission for a completely statistical process) accompanied by considerable fragmentation of the excited C_{60}^{q+}.

The fs pump-probe technique provides a direct access to the dynamics of the energy coupling. The relaxation pathways of laser excited C_{60} in a pump-probe experiments are very schematically depicted in Fig. 9.1. Considering a relatively weak (in a sense described in Sec. 3.2) pump pulse, one expects the energy to be deposited into the electronic and vibrational system of the neutral species, thus forming a highly excited, non-equilibrium population of states without significantly ionising the system. The following energy redistribution, i.e. "cooling" within the electronic system and coupling this energy into the nuclear degrees of

freedom of the neutral system is then monitored directly by a delayed probe pulse. Inelastic electron-electron scattering and electron-phonon coupling occurs on time scales τ_{el} from some tens to some hundreds of fs [CHH00, HHC03]. In previous studies such information was extracted rather indirectly from pulse duration dependent experiments. In contrast, fs pump-probe technique offers a more direct view into the dynamics with a temporal resolution of nuclear motion by analysing the time dependent signals of parent C_{60}^{q+} and fragment C_{60-2n}^{q+} ions. As schematically indicated in Fig. 9.1, these ions are generated by the probe pulse via MPI (i.e. immediately) or, respectively, after sequential evaporation of C_2 units on a time scale of ns to several μs.

9.2 Single Pulse Study

The mass spectra obtained with $9\,$fs laser pulses which were presented in Fig. 8.4a-e illustrate very interesting aspects of C_{60} fragmentation. Even for the highest intensity beyond saturation for C_{60}^{+}, the ion yield shows almost no singly charged fragments – in contrast to rich fragmentation observed for higher charge states. More insight into C_{60} fragmentation is gained from comparing the results measured with laser pulses of $9\,$fs and $27\,$fs duration, respectively. There, an intensity of $2.9 \times 10^{14}\,\mathrm{W/cm^2}$ for $9\,$fs pulses was used. This intensity roughly corresponds to the the saturation intensity for C_{60}^{+}. For comparison mass spectra for $27\,$fs have been measured at equivalent intensities according Eq. (8.23), assuming $N = 5, 8,$ and 11 for singly, doubly, and triply charged ions, respectively. The results are shown in Fig. 9.2 illustrating the dramatic influence of the laser pulse duration on the formation of fullerene-like fragments. Much less fragments are formed with $9\,$fs which clearly indicates that for shorter pulse duration the SAE picture becomes more and more applicable. Nevertheless, fragmentation is not negligible for higher charge states, especially not for $q > 2$. A similar trend has been seen in fast collision experiments [SHM99], where such interaction is regarded as a "δ-kick" on the electronic system by a strong transient Coulomb field leading to instantaneous electron emission and very little fragmentation.

Also, it is interesting to study the fragment ion yield with both pulse durations as a function of laser intensity. Fig. 9.3a-b present a log-log plot of the measured fullerene-like fragment ion yield $\sum C_{60-2n}^{q+}$ summed over all observed fragments, usually $1 \leq n \leq 6$, for final charge states

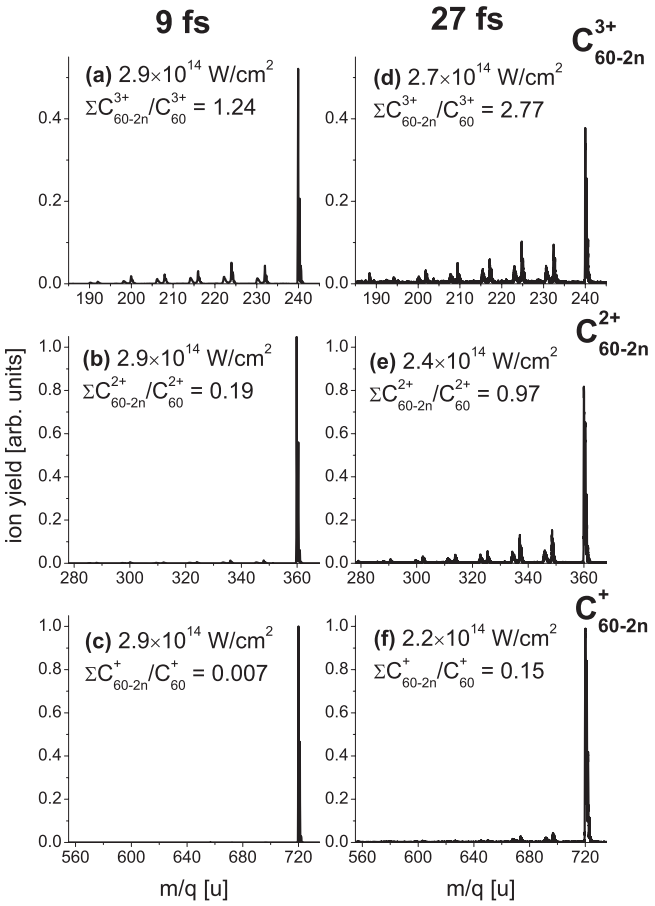

Figure 9.2: (a), (b), (c) Different parts of the C_{60} mass spectrum obtained with 9 fs laser pulses at 2.9×10^{14} W/cm^2. (d), (e), (f) The same parts of the mass spectrum but obtained with 27 fs laser pulses at equivalent intensities of 2.7×10^{14} W/cm^2, 2.4×10^{14} W/cm^2, and 2.2×10^{14} W/cm^2, respectively. The equivalent intensities are calculated according to Eq. (8.23). The data have been corrected for changing detection efficiencies of different charge states (see Sec. 4.5) and are normalised to the C_{60}^+ ion yield for each pulse duration.

$q = 1-3$. These data can not be fully interpreted in analogy to the parent ions using the same fit procedure applied there. However, a qualitative slope analysis of the log-log plot leads to slopes smaller than those for the parent ion yields of the same charge. This is quite interesting and may possibly indicate that ions are generated in such a way that they can easily absorb further so that the nuclear core can be heated efficiently. Saturation of fragment formation is reached in all cases between 2×10^{14} W/cm^2 and 3×10^{14} W/cm^2. This is approximately 2 or 3 times higher than for the respective parent ions, indicating that indeed many more photons are absorbed to heat the system prior to fragmentation.

In order to validate the above discussion quantitatively the fraction of fullerene-like frag-

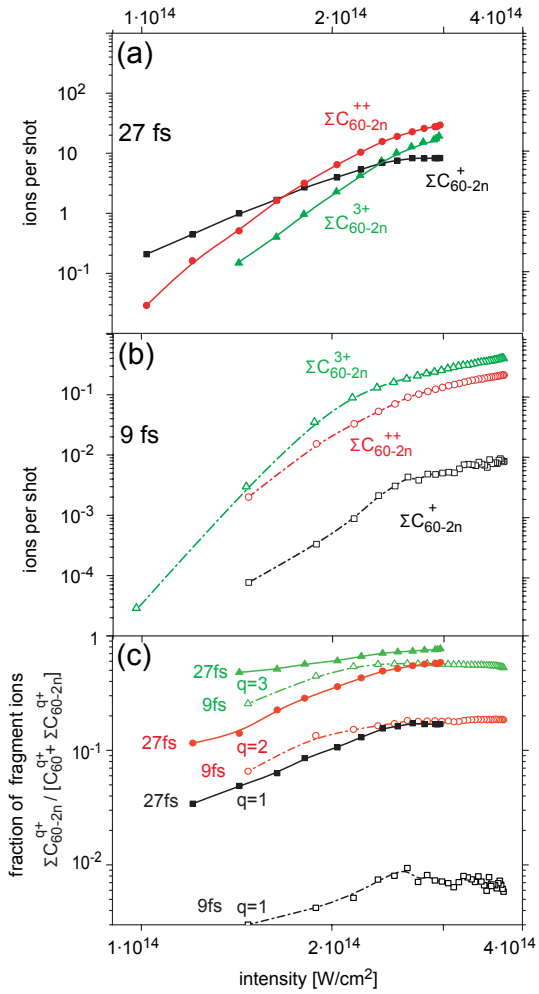

Figure 9.3: $\sum C^{+}_{60-2n}$, $\sum C^{2+}_{60-2n}$, $\sum C^{3+}_{60-2n}$ *fragment ion yield plotted as a function of the laser intensity on log-log scale: (a) obtained with* $27\,fs$ *and (b)* $9\,fs$ *laser pulses; (c) comparison of the fraction of fullerene-like fragment ions* $\sum C^{q+}_{60-2n} / \left[\sum C^{q+}_{60-2n} + C^{q+}_{60}\right]$ *as a function of laser intensity for different charge states and laser pulse durations.*

ment ions $\sum \mathrm{C}^{q+}_{60-2n}/(\sum \mathrm{C}^{q+}_{60-2n} + \mathrm{C}^{q+}_{60})$ is plotted as a function of laser intensity for different charge states and laser pulse durations. Such graph is shown in Fig. 9.3c. The fraction for $9\,$fs data is negligible ($< 1\%$) for singly charged fragments. In contrast, the fraction of triply charged fragments becomes as large as 60%. The fractions are 20% and about 80% for singly charged and triply charged fragments, respectively, when $27\,$fs laser pulses are used. Thus, two different pulse durations have fairly different impact on the C_{60} fragmentation. Moreover, it is clear that very different physical processes take place for $q = 1$ and $q = 3$. The simple message of Fig. 9.3 is that C^{q+}_{60} fragmentation is still significantly affected by changing the laser pulse duration from $9\,$fs to $27\,$fs. This is particulary true for final charge states $q > 1$, while

for $q = 1$ fragmentation is already reduced to a negligible amount at all intensities. Thus, for the formation of fragments with $q > 1$ the electron-electron interaction and as discussed in Sec. 8.2 the plasmon excitation [MCR08] play a key role in the energy redistribution.

9.3 One Colour Pump-Probe Study

To directly observe fingerprints of multielectron effects (MAE/NMED) in the initial excitation step of C_{60} one colour pump-probe mass spectrometry with 9 fs pulses is applied. The energy of the ultrashort pump pulse with an intensity of 7.9×10^{13} W/cm^2 is deposited into the electronic system during the ultrafast interaction. The delayed probe pulse of 6.8×10^{13} W/cm^2 is used to follow (probe) the energy redistribution among the electronic degrees of freedom.

Fig. 9.4a shows the normalised C_{60}^+ yield of the time resolved pump-probe measurement. Since the individual action of both pump and probe pulses on the C_{60} molecule leads to some ionisation at these intensities, the sum of single pulse signals has been subtracted from the resulting pump-probe yield. The simultaneously measured Xe^+ yield, which is also given in Fig. 9.4a, can be considered as an autocorrelation function because the ionisation of Xe atoms is a direct MPI process probably with a SAE determining the system ionisation.

The broadening of the C_{60}^+ trace at the bottom with respect to the Xe^+ signal indicates the presence of the MAE/NMED response [ZGe07]. As shown in Fig. 9.4b the total ion yield can be deconvoluted into two parts: a contribution from the direct MPI of C_{60} from the ground state (dark gray shaded) which essentially follows the Xe^+ signal and a significant contribution exhibiting dynamics on a sub-100 fs time scale (light gray shaded) which is slightly shifted towards positive time delays. The deviation of the C_{60}^+ pump-probe signal from the autocorrelation function may be interpreted as multielectron excitation of C_{60} during the laser interaction. According to recent theoretical calculations [TNE01, ZSG03, ZGe04] this is tentatively attributed to a finite probability to resonantly excite two or more electrons into the t_{1g} state which acts as a doorway to ionisation. The ionisation rate of C_{60} is determined by the excited electron density in the doorway state. This density depends on the laser intensity. Since the pump and probe pulses have slightly different intensities $(1.16 : 1)$, the ion distribution due to the excitation of the doorway state is shifted to positive time delays. The rough fit with two functions in each delay direction for the undelayed direct SAE/MPI process (proportional

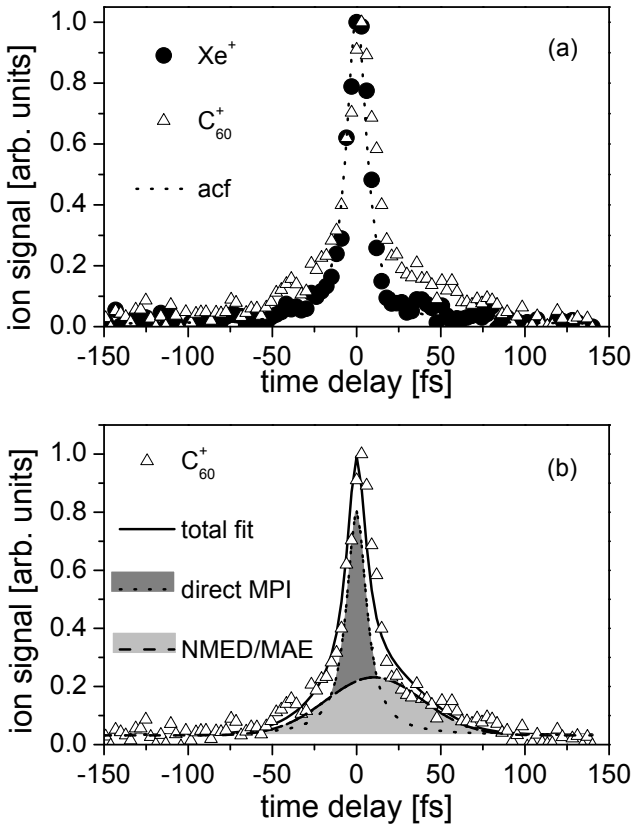

Figure 9.4: Results of one colour pump-probe experiment with 9 fs laser pulses. (a) C_{60}^{+} yield (open triangles) as a function of the time delay between pump (7.9×10^{13} W/cm^2) and probe (6.8×10^{13} W/cm^2) pulses. The ion yield is normalised to the maximum signal and zero delay is defined by the autocorrelation function (acf) (dotted line) derived from a fit of the simultaneously measured Xe^{+} signal (closed circles). (b) Contributions from direct SAE/MPI (dark gray shaded) and MAE/NMED (light gray shaded).

to the auto correlation signal) and the MAE/NMED (taken as an exponential delay) is used to estimate magnitudes of these two contributions. These contributions to the total C_{60}^{+} pump-probe signal are $\sim 65\%$ and $\sim 35\%$ for the SAE and NMED processes, respectively.

9.4 Two Colour Pump-Probe Study

Further studies of the energy redistributions pathways in C_{60} were performed using a two colour pump-probe technique. Results of time resolved mass spectrometry in a two colour pump-probe setup provide direct access to characteristic relaxation times. Mass spectra are

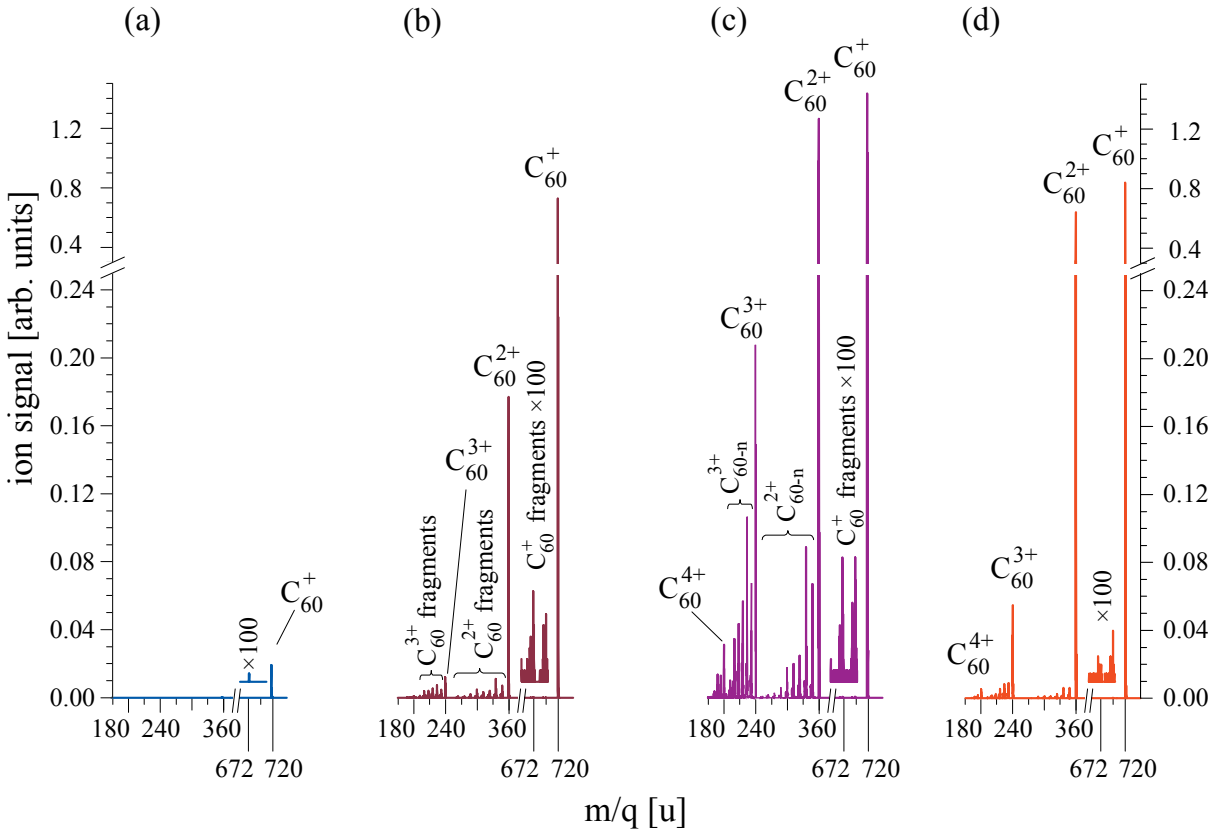

Figure 9.5: Mass spectra with blue (399 nm, 3.4×10^{12} W/cm^2) and/or red (797 nm, 5.1×10^{13} W/cm^2) laser pulses: (a) only the blue pulse is active; (b) the red pulse leads, blue follows, the time delay is 524 fs; (c) the blue pulse leads, red follows, the time delay is 29 fs corresponding to maximum signal; (d) only the red pulse is active. The small inserts for the C^+_{60-2n} fragments illustrate that these signals are extremely weak.

taken at varying delay times Δt_{br} between blue (399 nm) and red (797 nm) laser pulses ranging from -530 to 530 fs in step sizes of 6.7 fs. From these, transient ion signals are derived by integration over the full area of the individual mass peaks for parent C_{60}^{q+} and fragment C_{60-2n}^{q+} ions of charge states $1 \leq q \leq 4$ (for parents up to $q = 5$). For positive Δt_{br} the blue pulse leads, the red pulse follows – and vice versa for negative delays.

Fig. 9.5a-d show typical mass spectra in these pump-probe experiments. The intensity of the blue laser pulse is chosen such that the ion signals are nearly vanishing. Only a very weak C_{60}^+ signal is seen in the mass spectrum obtained with the blue only pulse as shown in Fig. 9.5a. In contrast, C_{60} interaction with only the (significantly more intense) red laser pulse leads to substantial ion signals, dominated by parent ions C_{60}^{q+} ($q = 1 - 4$) as presented in Fig. 9.5d. The pattern changes significantly when red and blue pulses are combined. If the red pulse hits

C_{60} prior to the blue pulse, the parent signals decrease in favour of the smaller fragments down to C_{44}^{q+} ($q \geq 2$), i.e. fragmentation is clearly enhanced by the additional blue pulse (Fig. 9.5b). However, the most dramatic change in the mass spectra is detected when the blue pulse comes first. In this case, as it is shown in Fig. 9.5c, all parent ions are significantly enhanced and the fragment C_{60-2n}^{q+} signals increase by a factor of up to 15.

Fig. 9.6a-d show the integrated ion yield for parent ions C_{60}^{q+} ($q = 1 - 4$) as a function of time delay Δt_{br} between 399 nm pump and 797 nm probe pulses. Fig. 9.7a-d show the analogue transients for some selected fullerene-like fragments C_{60-2n}^{3+}, $n = 0 - 3$. The transient spectra show ion yields as a function of time delay from -530 fs to 530 fs with a step size of 6.7 fs. For positive delays the blue pump pulse leads and the red probe pulse follows and for the negative delays vice versa. As already mentioned, the relatively weak blue pulse intensity of 3.4×10^{12} W/cm^2 was adjusted in such a way that the ultrashort radiation excites the electronic system via the resonant t_{1g} state without inducing significant ionisation and fragmentation as seen by the nearly negligible "blue-only" contributions (navy-blue long dashed lines) in Fig. 9.6 and Fig. 9.7. Only for C_{60}^{+} shown in Fig. 9.6a it can be distinguished from zero for $\Delta t_{br} \ll 0$. On the other hand, the red probe pulse of 5.1×10^{13} W/cm^2 already causes some ionisation and fragmentation even without pre-excitation by the blue pump pulse. This is indicated in Fig. 9.6 and Fig. 9.7 by red long dashed lines for $\Delta t_{br} \gg 0$.

The pump pulse resonantly pre-excites the electronic system via the first dipole allowed LUMO+1 (t_{1g}) state. This induces a highly non-equilibrium distribution of excited electrons in neutral C_{60}. Efficient population of the LUMO+1 (t_{1g}) "doorway" state is obviously a rate limiting step for depositing energy into the system. A laser pulse of relatively moderate intensity can initiate multielectron excitation when tuned into resonance [ZSG03, ZGe04]. This excitation prepares the neutral C_{60} molecules in a specially favourable state from which absorption of probe pulse photons into highly excited vibrational states of the ions may proceed. The thus prepared sample of excited neutral C_{60} molecules consists of a multitude of microcanonical ensembles with different total energies which initially are not in thermal equilibrium. Each of these microcanonical ensembles will have a specific characteristic relaxation time τ_{el} and a particular preference to finally end as a specific product, such as a parent C_{60}^{q+} or fragment ion C_{60-2n}^{q+}. The second delayed probe pulse monitors relaxation process of the coupling to electronic and vibrational degrees of freedom. The combined action of the weak blue and

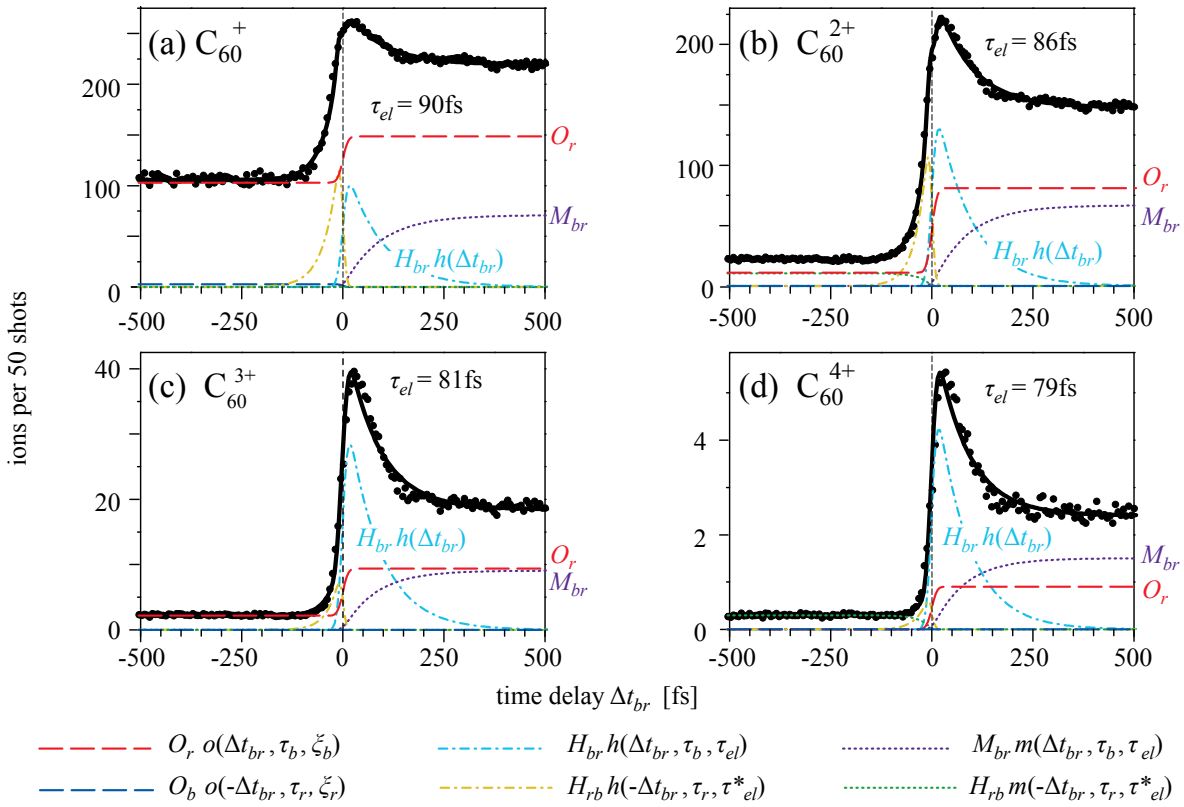

Figure 9.6: Total ion yield of (a) C_{60}^{+}, (b) C_{60}^{2+}, (c) C_{60}^{3+}, and (d) C_{60}^{4+} as a function of the time delay Δt_{br} between 399 nm pump pulse (3.4×10^{12} W/cm^2) and 797 nm probe pulse (5.1×10^{13} W/cm^2). Zero delay has been determined from MPI in Xe and indicated by the vertical black dashed line. At positive delay times the blue pulse comes first, the red follows, while the opposite holds for negative delay times. The transient ion signals are fitted (full black line) according to the fitting function with individual contributions indicated in the legend and described in the text.

strong red pulses has mainly tree effects on the formation dynamics of parent and fullerene-like fragment ions: (i) The red probe pulse only can already create significant ion signals. However, if the blue pulse follows ($\Delta t_{br} \leq 0$), it reduces the ion signals due to excitation of these ions, thus initiating subsequent ion fragmentation on the ns and μs time scale. (ii) The pump pulse generates highly excited electrons in the neutral system. They thermalise rapidly through inelastic scattering among the electronic degrees of freedom and coupling to the nuclear motion on a time scale τ_{el} (the relaxation time of the respective highly excited neutral parent). When the red probe pulse comes the system is ionised from highly excited states particularly efficiently (large transition dipole moments or/and Franck-Condon factors). Hence, the ion yields increase dramatically and maximum ionisation is found at $\Delta t_{br} \simeq 30 - 70$ fs. (iii) With the same time constant τ_{el} a thermalised (medium hot) electron population builds up and can

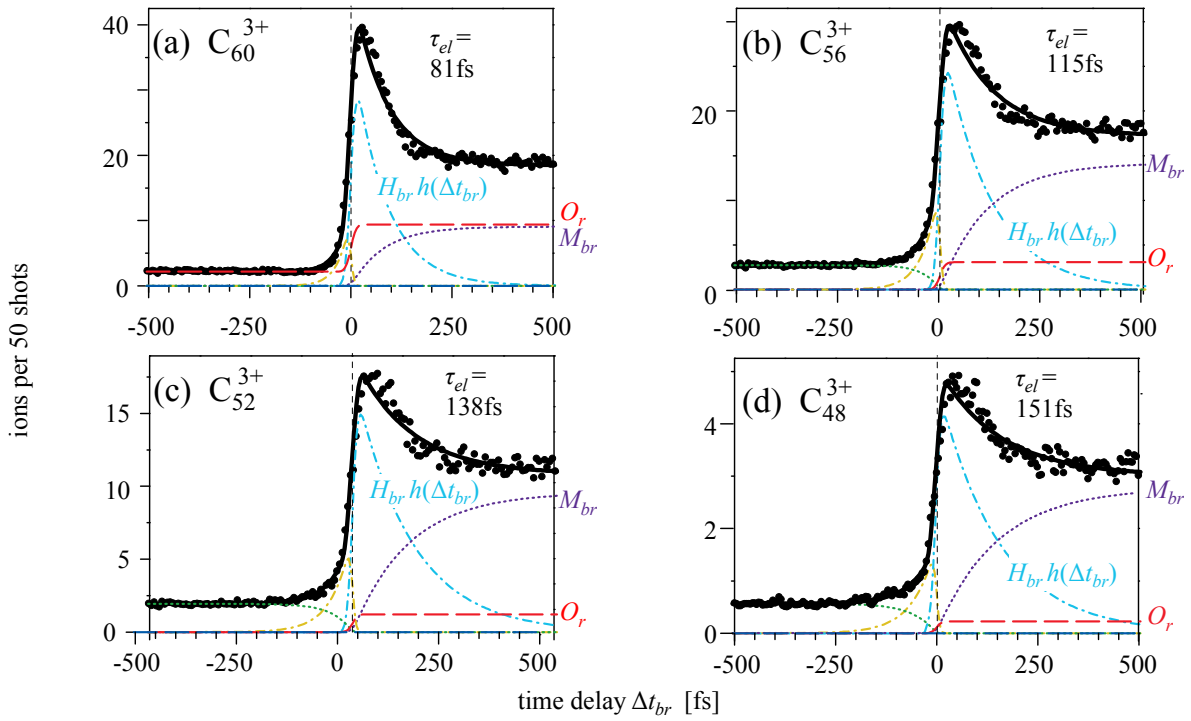

Figure 9.7: Total ion yield of (a) C_{60}^{3+}, (b) C_{56}^{3+}, (c) C_{52}^{3+}, and (d) C_{48}^{3+} as a function of the time delay Δt_{br} between 399 nm pump pulse (3.4×10^{12} W/cm^2) and 797 nm probe pulse (5.1×10^{13} W/cm^2). Otherwise as Fig. 9.6.

also be ionised by the red probe pulse. In this situation the ionisation probability is somewhat lower for these medium energy electrons but still higher though than for direct ionisation from the ground state.

For a quantitative comparison of the observed transients a fit function based on three components corresponding to the above described effects is used. The first contribution $o(\Delta t_{br}, \tau_{probe}, O_{pump}, \xi_{probe})$ takes into account ions that are formed in the single pulse interaction with pump and probe only illumination, as well as the effect of probe pulses reducing the ion yield compare to the pump only situation

$$o(\Delta t_{br}, \tau_{probe}, O_{pump}, \xi_{probe}) = \frac{1}{2}\left(O_{pump} - \xi_{probe}\right) \mathrm{erf}\left[-\frac{2\sqrt{\ln 2}\Delta t_{br}}{\tau_{probe}}\right] + \\ + \frac{1}{2}\left(O_{pump} + \xi_{probe}\right) \quad , \tag{9.1}$$

where O_{pump} is the experimentally determined signal produced by the pump pulse alone and $O_{pump} - \xi_{probe}$ describes the ion reduction due to the action of the probe pulse. The second contribution $h(\Delta t_{br}, \tau_{pump}, \tau_{el})$ to the ion signal arises from the "highly excited" electron

distribution. This signal is given by a convolution of the pump Gaussian pulse of τ_{pump} duration (FWHM) with an exponential decay function

$$h(\Delta t_{br}, \tau_{pump}, \tau_{el}) = \frac{1}{4}\sqrt{\frac{\pi}{\ln 2}}\tau_{pump} \exp\left[-\frac{\Delta t_{br}}{\tau_{el}} + \frac{\tau_{pump}^2}{16 \ln 2 \tau_{el}^2}\right] \times \\ \times \left(1 + \mathrm{erf}\left[\frac{2\sqrt{\ln 2}\Delta t_{br}}{\tau_{pump}} - \frac{\tau_{pump}}{4\sqrt{\ln 2}\tau_{el}}\right]\right) \quad , \tag{9.2}$$

where τ_{el} denotes the electron relaxation time constant. The third contribution $m(\Delta t_{br}, \tau_{pump}, \tau_{el})$ arises from the "thermalised" electron distribution which builds up with the same time constant τ_{el}. This signal follows the convolution of the Gaussian with the corresponding exponential rise function according to

$$m(\Delta t_{br}, \tau_{pump}, \tau_{el}) = \frac{1}{4}\sqrt{\frac{\pi}{\ln 2}}\tau_{pump}\left(1 + \mathrm{erf}\left[\frac{2\sqrt{\ln 2}\Delta t_{br}}{\tau_{pump}}\right]\right) - h(\Delta t_{br}, \tau_{pump}, \tau_{el}) \quad . \tag{9.3}$$

Finally, assuming that the blue and red pulses are pump and probe, respectively on positive time delays and vice versa on negative time delays, the fitness function can be written as

$$f(\Delta t_{br}) = o(\Delta t_{br}, \tau_r, O_b, \xi_r) + H_{br}h(\Delta t_{br}, \tau_b, \tau_{el}) + M_{br}m(\Delta t_{br}, \tau_b, \tau_{el}) + \\ + o(-\Delta t_{br}, \tau_b, O_r, \xi_b) + H_{rb}h(-\Delta t_{br}, \tau_r, \tau_{el}^*) + M_{rb}m(-\Delta t_{br}, \tau_r, \tau_{el}^*) \quad , \tag{9.4}$$

where the parameters H_{br}, M_{br}, H_{rb}, and M_{rb} are giving the fraction of the different processes, τ_b and τ_r are the duration of the blue and red pulses, respectively, τ_{el} and τ_{el}^* are the electron relaxation time constant, when the blue and red pulses are used as pump, respectively, O_b and O_r are the experimentally determined signals produced by the blue and red pulses alone, respectively, $O_b - \xi_r$ and $O_r - \xi_b$ describe the ion reduction due to the action of the probe red pulse and the probe blue pulse, respectively.

The contributions $o(\Delta t_{br}, \tau_r, O_b, \xi_r)$, $h(\Delta t_{br}, \tau_b, \tau_{el})$, and $m(\Delta t_{br}, \tau_b, \tau_{el})$ describe the dynamics at positive time delays, while $o(-\Delta t_{br}, \tau_b, O_r, \xi_b)$, $h(-\Delta t_{br}, \tau_r, \tau_{el}^*)$, and$m(-\Delta t_{br}, \tau_r, \tau_{el}^*)$ – at negative delays. The laser pulse durations of $\tau_b = 25\,\mathrm{fs}$ and $\tau_r = 27\,\mathrm{fs}$ for the blue and red pulses, respectively, are used for the fitting. The quantities H_{br}, M_{br}, H_{rb}, M_{rb}, τ_{el}, τ_{el}^*, ξ_r and ξ_b are fitted to the experimental data. τ_{el}^* is found to be very similar to τ_{el} but it is determined with much less accuracy due to the statistic of the data. Also, O_b and ξ_r are essentially zero and H_{rb} as well as M_{rb} are significantly smaller than H_{br} and M_{br}, respectively. In the following only the dynamic behaviour for positive time delays, where the relative weak blue pulse exclusive excites the electronic system, will be considered. In this case, the energy

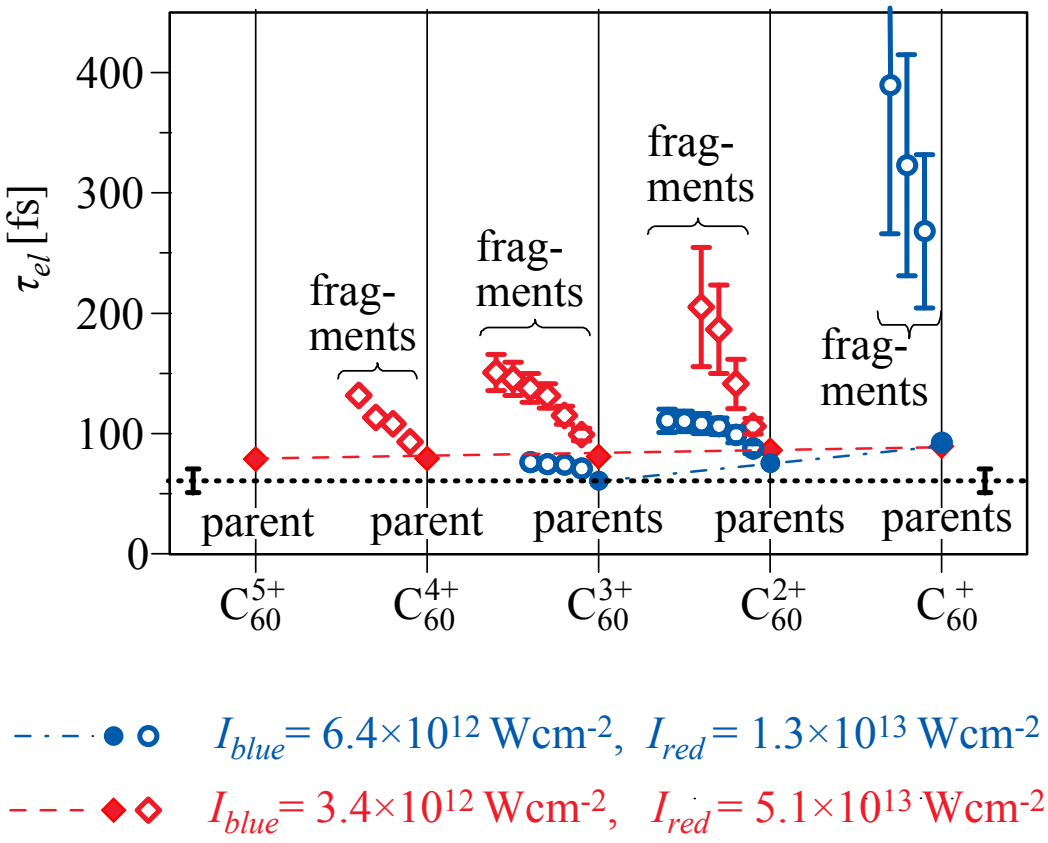

Figure 9.8: Relaxation times τ_{el} for highly excited electrons due to electron-electron and electron-vibrational coupling as determined from fitting the transient signals shown in Fig. 9.6 and Fig. 9.7. Two sets of data for different pump and probe laser intensities (I_{blue} and I_{red}, respectively) have been evaluated as noted in the legend. The dotted line (with error bar) indicates the electronic relaxation time for C_{60} derived in previous studies [CHH00, HHC03, SLS06], while dashed and dash-dotted lines are drawn to guide the eye.

redistribution process is directly monitored by the recording ion yields, whereas in the case of negative time delays, it is a priori not clear if initially formed charged species are further ionised and/or dissociated in the probe step. The discussion on the physics to be gleaned from these data focusses on two quantities: on the relaxation time τ_{el} and on the relative contribution from highly excited and thermalised, medium energy electrons, specifically on H_{br}/M_{br}.

The results obtained from fitting the transient signals of parent ions and of fullerene-like fragment ions are summarised in Fig. 9.8 and Fig. 9.9 for two different combinations of pump and probe pulses intensities. The first set of laser intensities corresponds to $I_{blue} = 3.4 \times 10^{12}\,\mathrm{W/cm^2}$ and $I_{red} = 5.1 \times 10^{13}\,\mathrm{W/cm^2}$. Under these conditions the blue only signal was practically zero, while the red only signal was quite substantial. The second set of

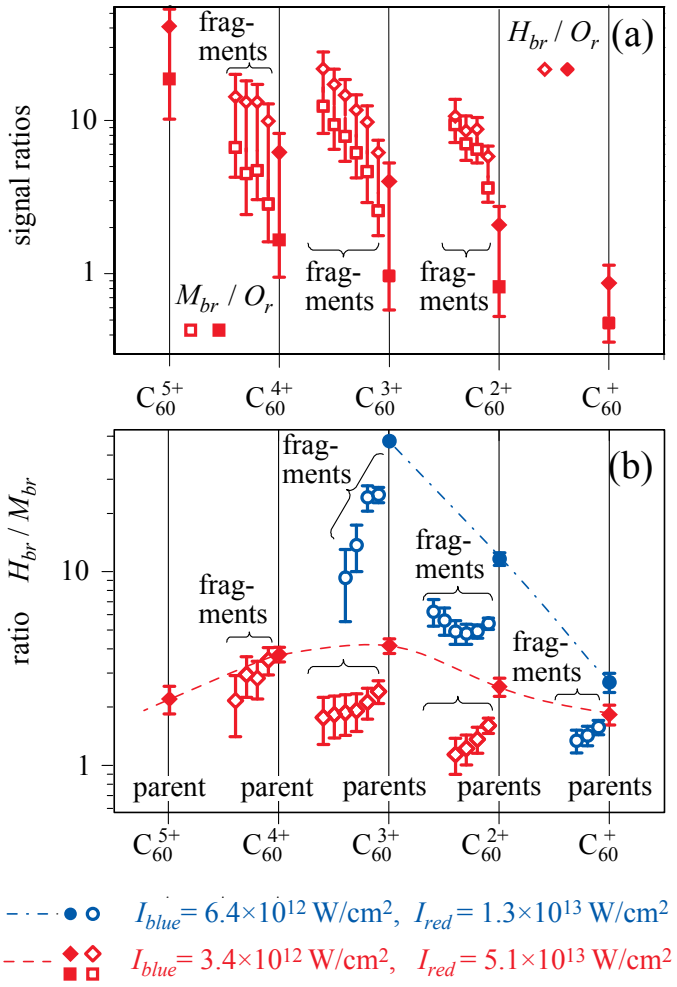

Figure 9.9: (a) Ratios H_{br}/O_r and H_{br}/O_r of additional ion yields from highly excited ($\propto H_{br}$) and thermalised ($\propto M_{br}$) medium energy electrons to the red only signal ($\propto O_r$). (b) Ratios H_{br}/M_{br} of ion yields from highly excited to those from thermalised electrons. Otherwise as Fig. 9.8.

parameters is $I_{blue} = 6.4 \times 10^{12}\,\mathrm{W/cm^2}$ and $I_{red} = 1.3 \times 10^{13}\,\mathrm{W/cm^2}$. At these conditions the blue only signals were still small but not negligible, while no red only signals were observed.

Fig. 9.8 shows the characteristic electron relaxation time constants τ_{el} for the various parent and fragment ions of different charge states. Several trends may be identified here: (i) The higher the pump pulse intensity and (ii) the higher the detected charge state of parent ions C_{60}^{q+} $(q = 1-5)$, the faster is the relaxation process. The lowest value observed here is $\tau_{el} \simeq 60\,\mathrm{fs}$ for C_{60}^{3+} with $I_{blue} = 6.4\times10^{12}\,\mathrm{W/cm^2}$ and $I_{red} = 1.3\times10^{13}\,\mathrm{W/cm^2}$. (iii) Fragments with an increasing number of evaporated C_2 units originate from microcanonical ensembles with increasing τ_{el}, i.e. from those with the smallest amount of excess electron energy. (iv)

Singly charged fragments – if detected at all – originate from microcanonical ensembles with particularly long thermalisation times. The longest relaxation time $\tau_{el} \simeq 400$ fs is observed for C_{54}^+.

To understand these trends one may refer to the relation between excess electron energy and electron-electron collision time in the Landau theory of Fermi liquid (LTFL) (see Sec. 3.3). The general trend found in the LTFL can be applied to free the C_{60} molecule: the higher the excess electron energy, the faster the relaxation of very highly excited electrons. The formation of multiple charged parent ions requires a precursor with as little vibrational energy as possible. These ensembles with the lowest vibrational excitation correspond to the highest electronic excitation and thus to the fastest relaxation. Therefore, τ_{el} are smallest for the parent ions. The longer relaxation times corresponding to smaller fragments can be explained by the same argument. The corresponding precursor ensembles are born with increasing vibrationally excitation, hence, with decreasing electronic excitation and thus have longer relaxation times. The trend with blue pulse intensity just emphasises these observations: higher blue intensity corresponds to more electronic at the cost of vibrational excitation, hence, faster relaxation of the precursor ensemble. The derived coupling time constants below 125 fs in the formation of multiply charged fragments C_{60-2n}^{q+}, $q > 1$ at $I_{blue} = 6.4 \times 10^{12}$ W/cm^2 are significantly different from those related to singly charged fragments which reach values up to 400 fs. Obviously, the formation of multiply charged fragments proceeds in a considerably different way. The very long relaxation times observed for C_{60-2n}^+ fragments indicate that in this case the precursor has a particularly low electronic energy. Hence, the probability for accessing the plasmon state by the red probe photon is particular low. All other neutral ensembles with some excess electronic energy content just have a very high chance to be transferred through the plasmon state into multiply charged ions. This is in agreement with the experimental results discussed in Sec. 8.2, where the importance of the C_{60} giant plasmon resonance for the formation of multiple charged species was demonstrated.

Additional information about the ionisation and fragmentation processes can be gained by analysing also the ion yield parameters derived from the measured pump-probe transient ion signals. Fig. 9.9 illustrates the relative importance of the signal enhancement due highly excited (H_{br}) and medium energy electrons (M_{br}). For simplicity of comparison Fig. 9.9a shows their ratio to "the red only" signal (O_r). The ratio H_{br}/M_{br} is presented in Fig. 9.9b. According

to Fig. 9.9a the higher the precursor excitation is the more pronounced for the enhancement of ionisation and fragmentation by blue pre-excitation in comparison to the "red only" signal: highly excited microcanonical ensembles obviously have a larger ionisation cross-section which enhances both fragments and parents. Fig. 9.9b shows the relative magnitude H_{br}/M_{br} of the relaxation which is obviously higher if the initial energy and density of the excited electrons are higher, i.e. for the more intense blue pulse. Fragments arise again from those ensembles with a high average vibrational energy. Thus, there is less electronic excitation density to relax and the ratio H_{br}/M_{br} naturally gets smaller. This supports the conclusion that fragmentation originates from species which are vibrationally excited but electronically rather cold. Therefore, this amplitude ratio drops as more and more C_2 units can evaporate since they belong to an initially higher vibrational energy content.

9.5 Pulse Shaping Study

This section is dedicated to the active control of the molecular response with judiciously tailored laser pulses. This powerful technique allows one both to maximise a specific, selected reaction and to learn about the the excitation and relaxation processes in molecules itself.

Since the formation of higher charged fragments is strongly intensity dependent (see Fig. 9.3), single charge fragments are used for the optimisation procedure. The maximisation of C_{50}^+ formation is chosen as prime aim of present study because this process can be considered as a measure for the temperature of the nuclear backbone. The optimal criterion (fitness function f) is simply defined as

$$f = S(C_{50}^+) \quad , \tag{9.5}$$

where $S(C_{50}^+)$ is the yield of C_{50}^+ ion. Fig. 9.10a illustrates a typical learning curve for the maximisation of C_{50}^+ formation. The algorithm of finding the optimal pulse shape is described in Chapter 7. For free optimisations the spectral phase was specified at 32 equidistant wavelengths between which a spline interpolation was used to build all 640 points. This turned out to be a good compromise for approximating the global maximum in solution space, while keeping the number of free parameters small and the convergence time short. The optimisation starts with 20 randomly chosen phase masks ($1^{st}\,generation$ in Fig. 9.10a). Usually,

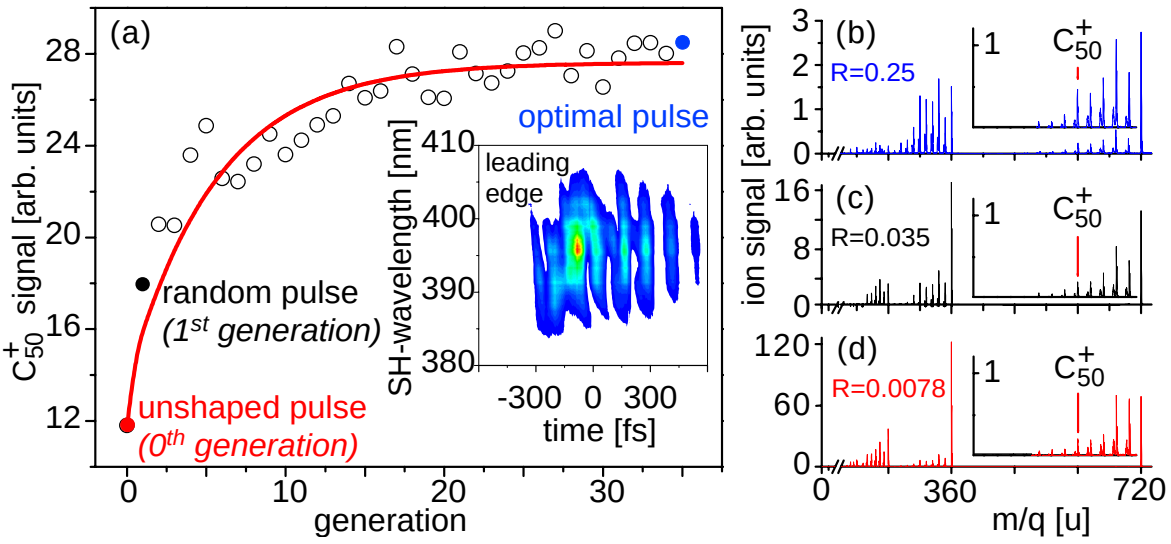

Figure 9.10: (a) C_{50}^{+} signal as a function of generation of the evolutionary algorithm. The inset shows the SH-XFROG map of the optimal solution. On the right, mass spectra recorded with optimal pulse (b), stretched to 340 fs pulse (c), and unshaped pulse of 31 fs FWHM (d) are plotted. The derived ratios $R = C_{50}^{+}/C_{60}^{+}$ are given.

convergence of the optimisation algorithm is achieved after $30 - 40$ generations. During the optimisation the ion signal of C_{50}^{+} increased by a factor of $\simeq 2.4$ compared to the signal recorded with unshaped pulse (0^{th} *generation* in Fig. 9.10a). In this particular case the energy of the 31 fs laser pulse at 797 mn central wavelength was $220\,\mu$J. The final, optimal pulse is characterised by the cross-correlation frequency resolved optical gating (SH-XFROG). The SH-XFROG map of the optimal pulse is shown on inset in Fig. 9.10a. The leading edge of the optimal pulse (the part which interacts with the C_{60} molecule first) is on the left. This map clearly shows that a sequence of several pulses is best suited for the formation of C_{50}^{+}. Although the shape of the optimal pulse change slightly from one optimisation to another, the pulse presented in Fig. 9.10a is representative of the majority ($\sim 90\%$) of optimal pulse shapes resulting from different optimisation runs.

To prove whether the structure of the optimal pulse is significant or simply acts as a stretched pulse, a mass spectrum obtained with a stretched pulse of the same overall energy and duration as the optimal pulse was recorded. This is illustrated in Fig. 9.10c. The yield of C_{50}^{+} with optimal pulse as shown in Fig. 9.10b is more than two times stronger compare to the yield with the stretched pulse. The ratio $R = C_{50}^{+}/C_{60}^{+}$ with the optimal pulse even increase by factors of 7 and 32 compared to those of the stretched and the unshaped pulse, respectively.

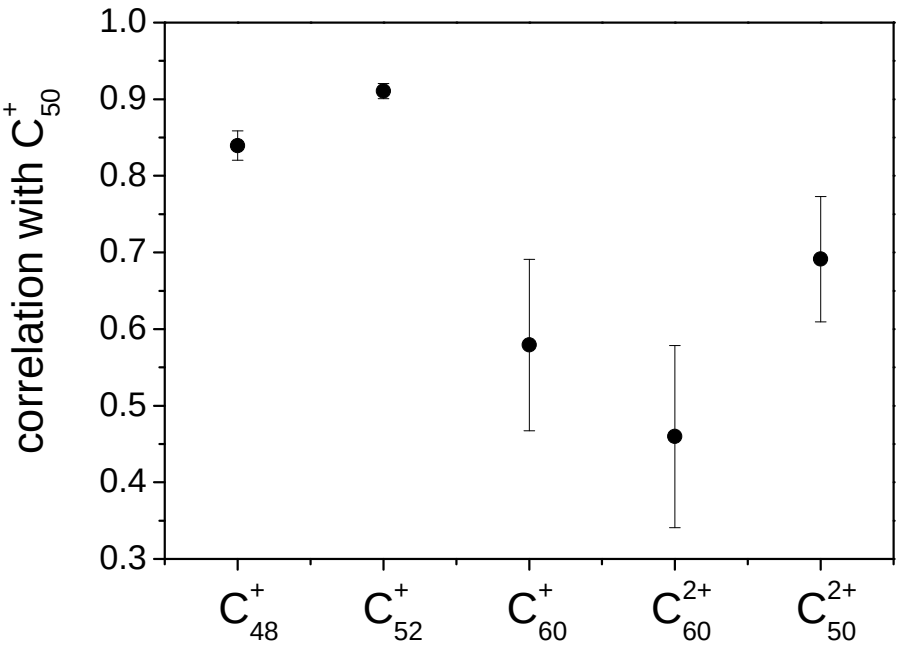

Figure 9.11: Correlation between C_{50}^+ and C_{48}^+, C_{52}^+, C_{60}^+, C_{60}^{2+}, and C_{50}^{2+} ions during the optimisation run. Each point is obtained by the averaging over the 16 individual optimisation runs.

During each optimisation run correlations between the formation of C_{50}^+ and other ions are recorded. Fig. 9.11 illustrates the correlations between C_{50}^+ and C_{48}^+, C_{52}^+, C_{60}^+, C_{60}^{2+}, and C_{50}^{2+} ions during the optimisation run. Each point is obtained by the averaging over the 16 individual optimisation runs. A strong correlation with the neighbouring fragments C_{48}^+ and C_{52}^+ is observed. On the other hand, a correlation with parent ion as well as with doubly charged ions is much weaker if at all present. This is a clear indication that the formation of singly charged fragments and the formation of highly charged ions have different nature. The yield of highly charged ions is mainly affected by the applied laser intensity, while singly charged fragments are formed as a result of sequential evaporation of C_2 units from highly vibrationally excited C_{60} in a statistical process. Thus, present optimisation scheme allows one to maximise the process of energy flow into vibrational modes of C_{60}.

To find additional evidence of the results of the optimisation experiments, a two-colour pump-probe study was performed with a relatively weak 399 nm pump pulse. The dynamics of the energy redistribution is then probed by a time delayed 797 nm probe pulse. Fig. 9.12a

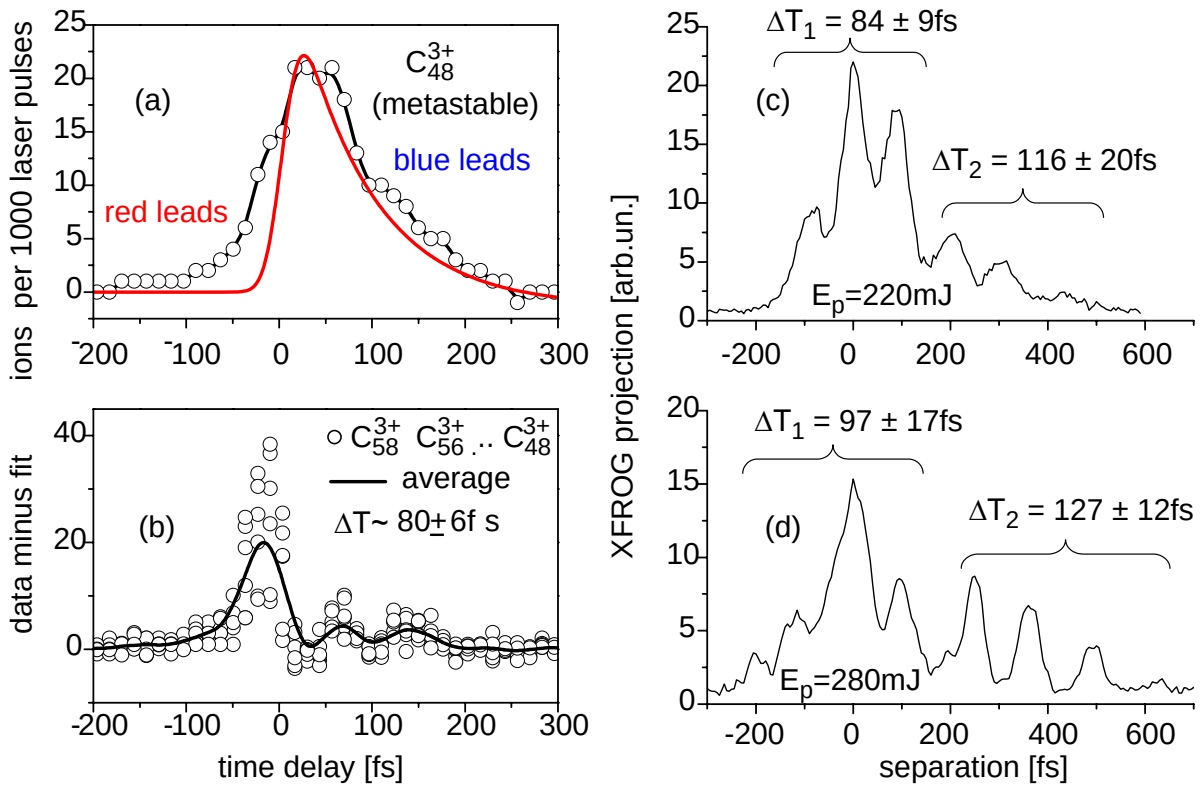

Figure 9.12: (a) Metastable C_{48}^{3+} ion signal as a function of time delay between blue pump and red probe pulses. An exponential decay is fitted to the data. (b) A modulation is found for all fullerene-like fragments C_{60-2n}^{3+} by subtracting the fits from the measured transients. (c) Optimised temporal shape with 220 μJ laser pulses and (d) 280 μJ pulses.

shows the metastable C_{48}^{3+} ion signal as a function of the time delay between 399 nm pump (1.7×10^{13} W/cm^2) and 797 nm probe pulse (7.3×10^{13} W/cm^2) with pulse durations of 25 fs and 27 fs, respectively. Triply charged, fullerene-like fragments were chosen because (i) they are most abundant using fs pulses as visible in Fig. 9.10d and (ii) metastable fragmentation (on a μs-ms timescale) is a particularly sensitive probe of the temperature of C_{60}^{q+} generated in the initial photo absorption process [HLS05]. At negative time delay, when the 797 nm pulse leads, almost no signal from C_{48}^{3+} is observed. Once pump and probe pulse overlap, the ion yield increases strongly and a maximum fragment signal is found at a positive delay of 50 fs. It can be concluded from this observation that the resonant pre-excitation of the t_{1g} doorway state by the 399 nm laser pulse significantly enhances multiple ionisation and massive fragmentation both induced by the subsequent 797 nm pulse.

Closer inspection of the pump-probe transient reveals a weak modulation on top of the C_{48}^{3+} ion signal. By fitting the data to the laser cross-correlation function convoluted with a single

exponential decay function and subtracting this from the measured signal, this modulation is found in all pump-probe data from multiply charged fullerene-like fragments with a periodicity of 80 ± 6 fs. This is shown in Fig. 9.12b. Obviously, nuclear rearrangement upon electronic excitation by the 399 nm pump pulse via the t_{1g} state occurs. The oscillation is then probed by the 797 nm probe pulse, assuming that the absorption cross-section for further energy deposition depends on the C_{60} oscillation.

The comparison of the pump-probe modulation with results from pulse shaping experiments (Fig. 9.10a) gives evidence that these different spectroscopic techniques probe very similar dynamics. Figs. 9.12c and 9.12d show the optimal temporal shapes for excitation with $220\,\mu$J and $280\,\mu$J pulses, respectively, derived by projecting the SH-XFROG maps onto the time axis. The key findings reproduced in several optimisation runs are the follows: (i) Each pulse shape consists of two distinct regimes with periodicity T_1 and T_2. (ii) The periodicity is smaller on the leading edge of the pulse than on the trailing edge ($T_1 < T_2$). (iii) It increases with increasing pulse energy. The observed values range from $T_1 = 84 \pm 9$ fs at $220\,\mu$J up to $T_2 = 127 \pm 12$ fs at $280\,\mu$J. All observed times including the pump-probe result are much larger than the well known radially symmetric breathing mode $a_g(1)$ of neutral C_{60} molecule which has an experimentally determined period of 67 fs [DZH93]. On the other hand, the observed periods are in general shorter than the lowest prolate-oblate mode $h_g(1)$ (122 fs [DZH93]) recently suggested as the dominantly excited mode of C_{60} due to the strong laser induced dipole forces acting in intense 1500 nm pulses [BCR03].

To get information on the nuclear motion excited in strong 400 nm and 800 nm laser fields theoretical calculations were performed using the so-called "non-adiabatic quantum molecular dynamics" (NA-QMD) [KSc03], developed recently. In this approach, electronic and vibrational degrees of freedom are treated simultaneously and self-consistently by combining time dependent density functional theory (TDDFT) in basis expansion with classical molecular dynamics.

The NA-QMD theory has already been successfully applied to excitation and fragmentation mechanisms in ion-fullerene collisions [KSc01] and laser induced molecular dynamics [HKS06]. Such kind of calculations is limited due to the computational effort by using the frozen core approximation and only a minimal basis set and thus describing the ionisation mechanism not very realistically. However, in principle it is possible to include the full ionisation process into

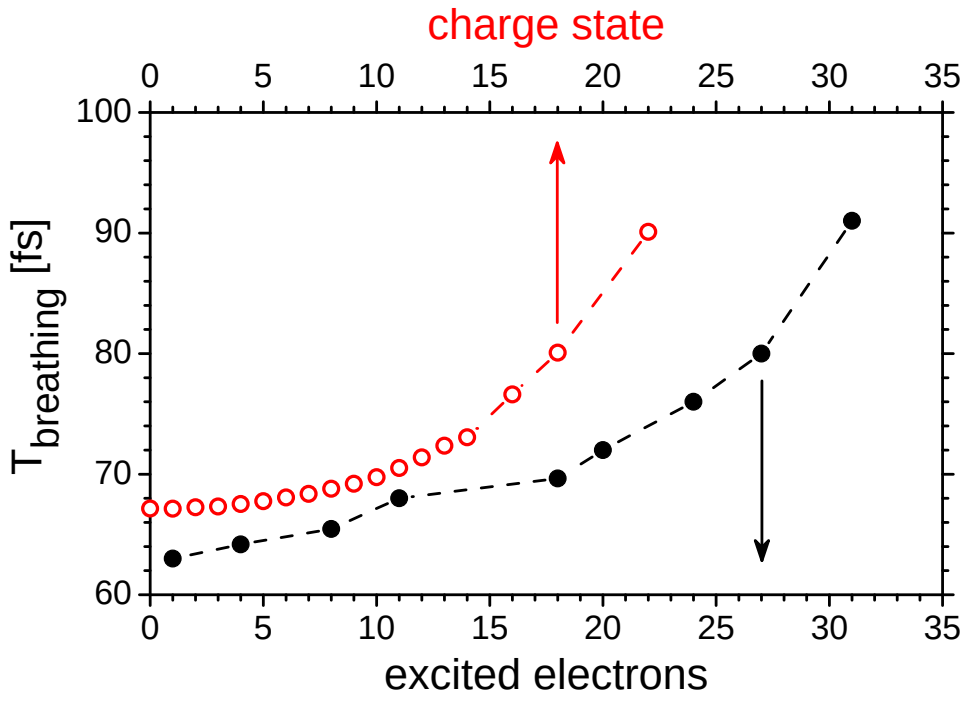

Figure 9.13: Period of the $a_g(1)$ breathing mode as a function of the number of excited electrons (black full circles) derived from NA-QMD simulations (laser parameters: $\lambda = 370\,nm$, $\tau = 27\,fs$, $I = 3.4 \times 10^{12} - 5.0 \times 10^{13}\ W/cm^2$) and as a function of C_{60} charge state (red open circles) derived from hybrid B3LYP level of the DFT method [SNS06].

NA-QMD, demanding however many more basis functions and a reliable absorber potential [UKS06].

In Fig. 9.13 (black full circles) results for exciting C_{60} by an intense laser field ($\lambda = 370\,$nm, $\tau = 27\,$fs, $I = 3.4 \times 10^{12} - 5.0 \times 10^{13}\,$W/cm^2) are presented. The wavelength of $370\,$nm is close to the experimentally used $399\,$nm pump pulse and matches the first optical resonance calculated in the local-density approximation (LDA). This calculation predicts an efficient excitation of many electrons by the laser field. At the highest laser intensity ($5 \times 10^{13}\,$W/cm^2) nearly 31 valence electrons are strongly excited resulting in an impulsive force that expands the molecule dramatically up to $9.4\,$Å which is 130% of the normal C_{60} diameter, orders of magnitude larger than expected for any standard harmonic oscillation. The new equilibrium position as well as the oscillation period of the $a_g(1)$ mode depend on the excited electronic configuration and thus on the absorbed energy. Fig. 9.13 shows a strong increase of the oscillation period with increasing number of absorbed electrons. The calculated oscillation period of highly excited C_{60} is in a good agreement with the results of the pump-probe

experiment presented in Fig. 9.12b as well as with the first time regime (T_1) of the optimally shaped laser pulse given in Fig. 9.12c-d. The longer periods seen experimentally in the second time regime (T_2) in Fig. 9.12c-d are not reproduced by the NA-QMD theory, possibly, because this time regime corresponds to the ionised C_{60}.

Indeed, the theoretical data derived from hybrid B3LYP level of the DFT method [SNS06] predict that the breathing mode period of the ionised C_{60} is increased in comparison with the neutral molecule. This is shown in Fig. 9.13 (red open circles), where the oscillation period of the $a_g(1)$ breathing mode is plotted as a function of different charge states q of C_{60}^{q+}. Coulomb repulsion between the charged carbon atoms may weaken the bonds in C_{60}^{q+}, hence, the oscillation period of the $a_g(1)$ breathing mode increases.